Acta Biomaterialia 209 (2026) 350–361

Contents lists available at ScienceDirect

Acta Biomaterialia

journal homepage: www.elsevier.com/locate/actbio

Full length article

Inter-spheroid proximity and matrix remodeling determine cancer associated fibroblast mediated cancer cell invasion

Pranav Mehta [a,b], Ankur Deep Bordoloi [b,e,*], Cor Ravensbergen [c], Ma.Kristen H. David [b], Wilma Mesker [d], Gerrit Jan Liefers [d], Peter ten Dijke [a,*], Pouyan E. Boukany [b,*]

[a] Department of Cell and Chemical Biology and Oncode Institute, Leiden University Medical Center, Leiden, the Netherlands
[b] Department of Chemical Engineering, Delft University of Technology, Van der Maasweg 9, 2629 HZ, Delft, the Netherlands
[c] Department of Pathology, Leiden University Medical Center, Leiden, the Netherlands
[d] Department of Surgery, Section Surgical Oncology, Leiden University Medical Center, Leiden, the Netherlands
[e] Aix-Marseille Université, CNRS, Centrale Méditerranée, IRPHE, UMR 7342, 13384 Marseille, France

ARTICLE INFO

Keywords:
Breast cancer
Cancer-associated fibroblasts (CAFs)
Collagen
Extracellular matrix (ECM)
Matrix remodeling
Cancer cell invasion
Heterogeneous spheroids

ABSTRACT

Breast cancer is the most commonly diagnosed malignancy worldwide, with molecular subtypes following distinct clinical trajectories. While Luminal A breast cancers are typically indolent, a subset enriched in α-smooth muscle actin (α-SMA)-positive cancer-associated fibroblasts (CAFs) exhibits aggressive behavior, facilitating tumor invasion. However, the biophysical mechanisms by which CAFs drive invasion and extracellular matrix (ECM) remodeling remain unclear. In addition, the temporal and spatial dynamics of CAF interactions with the collagen matrix and cancer cell spheroids remain unknown, raising the question of whether these processes follow a deterministic sequence or occur stochastically. To address this, we conducted histological analysis of Luminal A tumors, which revealed variation in CAF, cancer cell, and ECM organization at tumor boundaries. To assess the impact of CAF on cancer cell invasion, we use a 3D *in-vitro* model co-embedding 19TT breast CAF and MCF7 luminal breast cancer spheroids within a three-dimensional (3D) collagen-I hydrogel and performed time-lapse imaging. We demonstrate that inter-spheroid distance critically determines 19TT CAF-induced MCF7 spheroid behavior. Moreover, we showed that CAF-mediated collagen matrix remodeling and degradation precede the observed MCF7 spheroid disruption and are critical in promoting cancer cell spheroid expansion and cell dissemination. While broad-spectrum matrix metalloproteinase inhibition suppressed CAF-driven collagen degradation and MCF7 spheroid expansion, it did not prevent ECM remodeling, CAF migration, or single-cell dissemination of cancer cell spheroids. Furthermore, a complementary heterospheroid model revealed similar ECM remodeling and invasion dynamics despite the altered cellular arrangement of cancer cells and CAFs. Our findings enhance our understanding of the relationship between CAF activity and collagen matrix remodeling processes that promote cancer cell invasion, providing insights into the potential therapeutic benefits of targeting CAFs in breast cancer treatment.

Statement of Significance: This research provides key insights into breast cancer-associated fibroblasts (CAFs) mediated remodeling of the extracellular matrix (ECM) and subsequent breast cancer cell dissemination and invasion. Herein, we demonstrated that CAFs remodel collagen fibres before migration and matrix metalloproteinase (MMP)-mediated degradation. Using a 3D in-vitro model, we showed that distinct mechanisms govern cancer cell spheroid expansion and single-cell dissemination: while expansion depends on collagen matrix integrity, dissemination relies on CAF-driven collagen remodeling. These findings advance our understanding of the relationship between CAF activity and collagen matrix remodeling processes that promote cancer cell invasion, providing insights into the potential therapeutic benefits of targeting CAFs in breast cancer treatment.

* Corresponding authors.
E-mail addresses: ankur-deep.bordoloi@univ-amu.fr (A.D. Bordoloi), p.ten_dijke@lumc.nl (P. ten Dijke), p.e.boukany@tudelft.nl (P.E. Boukany).

https://doi.org/10.1016/j.actbio.2025.11.027
Received 16 April 2025; Received in revised form 28 October 2025; Accepted 17 November 2025
Available online 19 November 2025

1. Introduction

Breast cancer is one of the most commonly diagnosed cancers worldwide and comprises distinct molecular subtypes characterized by specific biomarkers and clinical features [1]. These subtypes arise from complex intra- and intercellular interactions driven by genetic mutations, epigenetic modifications, and dynamic crosstalk between cancer cells and their heterogeneous tumor microenvironment (TME) [2]. It has been established that Luminal A breast cancer - the most prevalent subtype - generally follows a more indolent course and has a favorable prognosis. However, a subset of Luminal A tumors associated with α-smooth muscle actin (α-SMA)-positive cancer-associated fibroblasts (CAFs) in the TME exhibit significantly aggressive behavior, leading to distant metastasis and relapse [3].

Within the TME, CAFs, along with other cellular components such as endothelial cells, immune cells, and the extracellular matrix (ECM), collectively constitute the tumor stroma. It has been shown that the stromal-to-tumor ratio serves as an independent prognostic indicator, with a higher stromal fraction correlating with increased tumor aggressiveness and poorer patient outcomes [4–6]. However, substantial variability across studies highlights the complexity of stromal contributions to tumor progression [4–9]. These discrepancies likely stem from the dynamic and reciprocal interactions between cancer cells and their stromal counterparts, leading to extensive reorganization of cellular composition and ECM architecture during tumorigenesis [10,11]. Consequently, these processes create a heterogeneous TME characterized by spatially distinct features, underscoring the need for a more refined analytical framework to accurately assess stromal contributions to disease progression. The inherent heterogeneity of the TME results in significant phenotypic diversity among cancer cells and CAFs, leading to unique functional signatures and cellular characteristics that vary across different regions of the TME [12].

In Luminal breast cancers, CAFs actively promote tumor progression by reprogramming cancer cells, thereby enhancing therapeutic resistance, disrupting cancer cell metabolism, and increasing cancer cell motility [13]. Direct physical interactions between CAFs and cancer cells further sustain these changes [13,14]. CAFs also exert considerable regulatory effects on the collagen ECM through mechanisms that modulate collagen cross-linking, deposition, and degradation [15]. Through secretion of matrix metalloproteinases (MMPs) and contractility-driven fiber realignment, CAFs both degrade and remodel the collagen ECM [16–20]. This biomechanical remodeling leads to the aggregation of thin collagen fibrils into thicker, aligned bundles - often termed “collagen highways” - which serve to facilitate and guide cancer cell migration and invasion [21].

As the TME undergoes temporal evolution, its ECM is gradually remodeled into a tumor-facilitating matrix due to the biophysical and biological activities of CAFs and cancer cells. These cells can modulate the biophysical and biochemical properties of the collagen ECM, leading to increased matrix stiffness, which is a notable characteristic of breast malignancy [22,23]. *In-vitro* models support these findings, showing that aligned collagen fibers increase matrix stiffness and enhance tumor cell migration efficiency by promoting directional persistence [24]. Together, these structural and mechanical changes promote tumor progression and therapeutic resistance [25]. Yet, the role of CAFs in indolent breast cancers, characterized by non-migratory cancer cells, and the mechanisms that may precipitate invasion and eventual metastasis in these settings remain unresolved. Specifically, the effects of CAF-induced matrix remodeling, along with its reciprocal influence on CAF-cancer cell interactions in indolent breast cancer, are not well defined. Recent advances in breast cancer research have emphasized that local ECM architecture at the TME boundary, along with the spatial organization of cancer cells and CAFs, significantly affects patient outcomes [26–30]. To address this, we studied the behavior of luminal breast cancer spheroids in a collagen matrix and ECM remodeling in the presence of breast cancer CAF spheroids. To mimic the heterogeneous architecture of breast tumors, we employed both dual-spheroid and heterospheroid assays. The dual-spheroid system captured the spatial compartmentalization often observed in breast cancers, in which CAF-rich stromal regions are partially or fully separated from epithelial tumor clusters [31,32]. By varying inter-spheroid distance, this system allows us to probe how stromal-epithelial proximity regulates invasion dynamics. Complementarily, we also considered a heterospheroid-model emulating intermixed epithelial-stromal regions, common in CAF-rich tumors. Our experimental findings enhance the understanding of the relationship between CAF activity and collagen matrix remodeling processes that promote cancer cell invasion, providing insights into the potential therapeutic benefits of targeting CAFs in breast cancer treatment.

2. Materials & methods

2.1. Cell culture and reagents

The human Luminal A epithelial breast cancer cell line MCF7 was purchased from American Type Culture Collection (ATCC). The human telomerase reverse transcriptase (hTERT)-immortalized breast 19TT CAFs have been previously described [33]. These cells were originally derived from invasive ductal carcinoma tissue and have been reported to constitutively express α-SMA in culture, representing a stable and pre-activated CAF population [33,34]. All cells were cultured in Dulbecco’s Modified Eagle Medium (DMEM), High Glucose (Sigma) containing 4.5 g/L glucose, l-glutamine, but without sodium pyruvate and supplemented with 10% fetal bovine serum (FBS, Sigma) and 1% antibiotic-antimycotic solution (Gibco). Cells were frequently tested for the absence of mycoplasma and checked for authenticity by short tandem repeat (STR) profiling.

2.2. Conditioned medium experiments

To generate conditioned medium (CM), 2×10^5 19TT-CAF cells were seeded per well in a 12-well plate and cultured in 1.5 mL of complete DMEM (composition as described in Section 2.1). After 48 hours, the supernatant was carefully collected and filtered through a 0.22 μm Millex^{TM} PVDF syringe filter (Sigma-Aldrich) and stored at 4°C until further use. For stimulation experiments, MCF7 spheroids were embedded in 3 mg/mL collagen gels and treated with 200 μL of 19TT CAF CM. Control spheroids were cultured in standard medium as described above (Section 2.1).

2.3. Pharmacological inhibition

Spheroids were treated with Batimastat (BB94, 30 μM; Selleckchem), E64 (10 μM; Tocris 5208), Blebbistatin (Bleb, 10 μM; Abcam ab120425), or Y-27632 (Y27, 10 μM; Tocris 1254). Batimastat powder was dissolved to 30 mM stock solution. E64 and Y-27 powders were dissolved to 1 mM stock solutions, and Blebbistatin to a 5 mM stock solution, all stored at -20°C until use. Working concentrations were prepared fresh by diluting stock solutions into culture medium according to the manufacturer’s instructions. Vehicle controls were included.

2.4. Lentiviral transduction

Constitutive expression of fluorescent markers was accomplished via lentiviral transduction. MCF7 cells were labeled with plv-mCherry, and 19TT CAFs were labeled with pLenti CMV H2B green fluorescent protein (GFP) Hygro (656-4). pLenti CMV GFP Hygro (656-4) was a gift from Eric Campeau & Paul Kaufman (Addgene plasmid #17446; http://n2t.net/addgene:17446; RRID:Addgene_17446). Lentiviruses were produced by co-transfecting cDNA expression plasmids with helper plasmids pCMV-VSVG, pMDLg-RRE (gag/pol), and pRSV-REV into HEK293T cells using polyethyleneimine (PEI). Cell supernatants were

harvested 48 hours after transfection and stored at -80°C. Cells were labeled by infecting for 24 hours with respective lentiviral supernatants diluted 1:1 with cell culture medium and 5 ng/ml of polybrene (Sigma-Aldrich). 48 hours after infection, 19TT CAFs were placed under Hygromycin-B (Thermo Fisher Scientific) selection, and MCF7 cells were placed under Neomycin (A1720, Sigma-Aldrich) selection. The fluorescently labeled cells were cultured with 100 μg/ml of the respective antibiotics to obtain stable fluorescent cell lines and maintain selection pressure.

2.5. Spheroid seeding and characterization

MCF7 and 19TT CAF spheroids were seeded in Corning Elplasia 96-well Round Bottom Ultra-Low Attachment (ULA) Microcavity Microplates (Corning, 4442). Briefly, cells were trypsinized (Trypsin-EDTA, Gibco™, 25200056) and resuspended to a concentration of 1×10^6 cells/ml. 40×10^3 (500 cells per microwell, 79 microwells) cells were seeded to produce 79 spheroids. Spheroids were ready after 48 hours of culture. MCF7 spheroids (200 ± 25μm diameter) and 19TT CAF spheroids (125 ± 25μm diameter) were used for invasion studies. MCF7 spheroids were cultured in DMEM, High Glucose (Sigma) containing 4.5 g/L glucose and l-glutamine but without sodium pyruvate and supplemented with 10% FBS (Sigma) and 1% antibiotic-antimycotic solution (Gibco). For 19TT CAF spheroids, a high-viscosity culture medium was made using methylcellulose as described previously [35]. Briefly, a 20% methylcellulose solution was prepared by sterilizing 6 g of methylcellulose in an autoclave. This was subsequently mixed with 250 ml of DMEM High Glucose. Once methylcellulose was dissolved, an additional 250 ml of DMEM High Glucose and 55ml FBS was added, and the solution was mixed overnight at 4°C. The following morning, the solution was centrifuged at 5000g for 2 hours at 4°C, and the supernatant was stored at 4°C until use.

19TT CAF - MCF7 heterogeneous spheroids (heterospheroids) were generated using the hanging drop method. Briefly, cells were trypsinized (Trypsin-EDTA, Gibco™, 25200056) and resuspended to a concentration of 1×10^3 cells/ml. Cell lines were mixed and diluted to a final concentration of 1000 cells / 30 μL, with 500 cells of each cell line. As described above, a high-viscosity culture medium containing 20% methylcellulose (M0512, Sigma), was used to culture cells. 30 μL droplets containing 1000 cells were cultured for 48 hours before the fully formed spheroids were harvested for experiments.

2.6. Preparation of collagen hydrogels

Collagen type-1 hydrogels were prepared on ice to prevent polymerization. Briefly, collagen (Corning™, 354249) was mixed with 10x Reconstitution Buffer (200 mM HEPES + 262 mM sodium bicarbonate) and 10x DMEM (Gibco™, 12100061) in an 8:1:1 ratio, adjusted to pH 7.4 using 0.5M NaOH, and diluted with sterile Milli-Q water to the required concentration (3 mg/ml) [36]. The hydrogel was incubated at 4°C for 20 minutes, followed by 37°C for 40 minutes.

2.7. Spheroid invasion experiments

A thin 100 μL collagen bed (3 mg/ml) was created and allowed to gel for the invasion experiment (as mentioned in section 2.4). This was followed by harvesting 19TT CAFs and MCF7 spheroids, mixing them with freshly prepared collagen, embedding them on top of the collagen bed, and incubating them as stated above. The culture medium was added after incubation, and the device was set up for time-lapse imaging. Initial imaging was performed ~1 hour after embedding (or immediately post-collagen gelation). This time point was designated as T_0 for all subsequent analyses in this study. The culture medium was refreshed every 48 hours for experiments running for up to 96 hours. Analysis was limited to spheroids (heterogeneous or dual-spheroid systems) that were at least 400 μm away from other spheroids. This ensured that no additional interactions would occur within the region of interest (ROI) for the experiment duration.

2.8. Time-lapse confocal and reflection imaging

Confocal fluorescence and reflection microscopy were performed using the Zeiss LSM-980 integrated with a live cell incubator. Temperature was maintained at 37°C and CO_2 at 5% during microscopy measurements. Images were collected at 2-hour intervals and analyzed using ImageJ2 (v2.14, National Institute of Health, USA) and custom Matrix Laboratory (MATLAB) scripts. For image acquisition, an EC Plan-Neofluar 10x/0.3NA M27 (Zeiss) air objective was combined with 13mW 488 nm and 543 nm lasers for fluorescence imaging. During acquisition, the digital gain was set to 1, the digital offset 0, laser power to 0.2%, and the master gain at 650V. Appropriate band-pass filters were used to prevent spectral overlap between GFP and mCherry channels. A 488 nm laser with a detection range of 476 nm to 502 nm was used for reflection microscopy. The master gain was set to 600 V, and 0.2% laser power was used during reflection imaging. The reflection images in the figures were collected with equivalent gain settings and presented with equivalent digital contrast, brightness, and levels. All images were acquired at an optical zoom of 1.0, with a field of view of 848.53 μm x 848.53 μm with 2048 × 2048 pixels. Z-stacks were acquired at a 20 μm step size for a total range of 400 μm.

2.9. Image processing

Carl Zeiss Image (CZI) files were extracted and saved as '.tiff' files after image acquisition using custom ImageJ scripts. Before analysis, these files were processed, during which the mean noise was subtracted from the images, and fluorescent channels (GFP and mCherry) were checked for spectral overlap.

2.9.1. Circularity and change in area of MCF7 spheroids

MCF7 spheroid images were extracted and saved as image sequences using custom ImageJ scripts. Maximum Z-projections were created to find the maximum diameter of the MCF7 spheroids. These maximum projections were then utilized with custom MATLAB scripts to binarize and threshold images to identify MCF7 spheroid edges. The in-built regionprops function was subsequently used to measure the change in area and circularity of spheroids. To calculate the shortest distance between MCF7 and 19TT CAF spheroids, image sequences in the Z-plane at T_0 were saved for each spheroid. Weighted centroids in three-dimensional (3D) space were computed based on the maximum spheroid area at each Z-plane. The 3D centroid-to-centroid distance was then determined. Using a nearest-neighbor algorithm, the coordinates of the intersection between the centroid-connecting line and the spheroid boundary were identified. These boundary coordinates for both spheroids were then used to calculate the shortest inter-spheroid distance.

2.9.2. Migration analysis

CAF spheroid migration was calculated by measuring the maximum cross-sectional spheroid area at T_0 (A_0) and during its culture within the collagen matrix (A_t). The invasive index was then defined as $\delta A = (A_t / A_0) - 1$ to quantify the level of invasion for different spheroids.

2.9.3. Collagen fiber orientation, void fraction and brightness characterization

Collagen fiber images obtained via reflection imaging were analyzed using ImageJ and customized MATLAB scripts. Collagen planes corresponding to the central spheroid plane were selected in ImageJ for further analysis. Spheroid area and position are segmented from the image using Gaussian filtering ($\sigma = 2$ pixels), morphological operations and Otsu's thresholding [37]. OrientationJ's vector field analysis is used to determine collagen fibers' local orientation and isotropy relative to

the absolute x-axis [38]. The size of the Gaussian kernel was set to 10 μm [38,39]. As shown in Fig. S1, the resulting orientation mask was analyzed in conjunction with intensity thresholded collagen masks using custom MATLAB scripts to identify, transform, and subsequently estimate the collagen fiber alignment relative to the centroids of the corresponding spheroids, providing a detailed spatial understanding of collagen architecture relative to spheroid positioning. To quantify collagen degradation, we extended our MATLAB script and used the intensity thresholded collagen masks to identify void spaces between collagen fibers based on relative pixel intensity values and calculate the void fraction (V_f) of the collagen plane. These V_f values were then normalized to the V_f value at T_0. To quantify the change in collagen fiber brightness (pixel intensity values), we summed up all pixel values of the collagen fibers at each time point (I_P) and normalized them by T_0.

2.10. Tissue sectioning, imaging and analysis

2.10.1. Tissue processing, histochemical staining, and digitization of human breast cancer

Formalin-fixed, paraffin-embedded tumor tissues were sectioned into four μm slides and processed sequentially, including deparaffinization with xylene, rehydration through an ethanol gradient, histological staining, air drying at room temperature, and mounting with a xylene-based medium (Permount; Thermo Fisher Scientific Inc., Waltham, Massachusetts, USA). For this study, a tissue block containing the most invasive tumor region, used for Tumor (T)-status assessment, was selected for preparation of serial sections. These sections were stained with hematoxylin and eosin (H&E) and Picrosirius red (PSR). PSR staining involved treatment with 0.1% Direct Red 80 dye in saturated picric acid (Sigma-Aldrich, Merck, Darmstadt, Germany) for 60 minutes, followed by rinsing in two changes of 0.5% glacial acetic acid (Avantor, Inc., Radnor Township, Pennsylvania, USA). Stained slides were digitized in brightfield mode using a Pannoramic 250 slide scanner (3DHISTECH, Budapest, Hungary) at 200 × magnification (0.39 μm/pixel) and saved as proprietary .mrxs files.

2.10.2. Fluorescent whole-slide imaging of picrosirius red-stained tissue sections

Picrosirius red-stained tissue sections were digitized in fluorescent mode using a Pannoramic 250 slide scanner (3DHISTECH, Budapest, Hungary) at 200 × magnification (0.39 μm/pixel) and saved as proprietary MIRAX (.mrxs) files. Tissue autofluorescence was captured using a Fluorescein isothiocyanate (FITC) filter cube (excitation: 460-488 nm, emission: 502-547 nm) with an exposure time of 800 ms. The fluorescence emission of the fibrous ECM stained by Sirius red was recorded using a Tetramethylrhodamine isothiocyanate (TRITC) filter cube (excitation: 532-554 nm, emission: 573-613 nm) with an exposure time of 44 ms.

2.10.3. Immunohistochemistry

For multiplex immunofluorescence, tissue sections were deparaffinized, rehydrated, and subjected to heat-induced epitope retrieval using citrate buffer (pH 6.0). To minimize non-specific binding, sections were incubated with 5% goat serum for 10 minutes at room temperature. Primary antibodies were applied overnight, including anti-αSMA (clone 1A4, DAKO, M0851, 1:300 dilution) and pan-cytokeratin (AE1/AE3, DAKO, M3515, 1:300 dilution). The next day, sections were incubated with Alexa Fluor-conjugated secondary antibodies: 647 goat anti-mouse IgG2a (Life Technologies, A21241, 1:200 dilution) and 546 goat anti-mouse IgG1 (Invitrogen, A21123, 1:200 dilution). All antibody incubations were performed for 30 minutes at room temperature in the dark. Finally, nuclei were counterstained with Hoechst 34580 (Sigma-Aldrich, 63493, 1:2000 dilution) for 5 minutes.

2.11. Statistical analysis

All graphs shown in this work were produced using GraphPad Prism. Statistical analyses were run within the software, and significance between groups was assessed using unpaired t-tests or ANOVA based on experiment variable dependencies. Statistical significance among more than two groups was assessed using ANOVA tests. Probability values less than 0.05 were deemed significant ($p < 0.05$ *, $p < 0.01$ **, $p < 0.001$ ***).

3. Results

3.1. Cancer cell and CAF distribution, and collagen morphology observed in luminal breast tumor sections

To explore the heterogeneity of the TME and the organization of the ECM in relatively indolent breast cancers, we analyzed tissue sections from Luminal A breast cancer samples. Our focus was on the collagen architecture and cellular organization at distinct tumor boundaries (Fig. 1 A-C). Analysis of multiple tumor boundaries across four samples revealed significant variability in the collagen fiber organization in the TME ECM. Some tumor boundaries displayed a thick collagen layer separating the TME from adjacent healthy tissues, while others were characterized by infiltrative collagen fiber projections extending into the surrounding tissue. Based on these structural differences, we classified tumor boundaries as either non-infiltrative or infiltrative tumor boundaries (Fig. 1B-C). Among the four tumor samples, CAF01 and CAF02 showed both infiltrative and non-infiltrative boundaries, CAF03 displayed only non-infiltrative margins, and CAF06 exhibited only infiltrative margins. The tumor shown in Fig. 1 (Tumor ID: CAF01) featured both infiltrative and non-infiltrative fronts, while the remaining sections are presented in Fig. S2. Infiltrative tumor fronts were marked by highly organized collagen fibers running perpendicularly to the tumor boundary and forming tracks or protrusions that extended into adjacent mammary fat tissue (Fig. 1A, blue arrows). In contrast, non-infiltrative fronts showed collagen fibers predominantly aligned parallel to the tumor border, delineating a continuous interface between tumor and surrounding tissue (Fig. 1A, red arrows).

Immunofluorescent staining for pan-cytokeratin (pCK), an epithelial marker identifying tumor cells, and α-SMA, a marker of activated fibroblasts (CAFs), revealed marked differences in stromal composition and organization between infiltrative and non-infiltrative tumor boundaries. In infiltrative regions (Fig. 1C, bottom panels), tumor cells appeared as dispersed clusters intermingled with α-SMA-positive fibroblasts, which were prominently localized at the tumor-stroma interface. Notably, both CAFs and collagen fibers (Fig. 1C, top panels) displayed an aligned orientation along the apparent invasion paths of the tumor cells. In contrast, non-infiltrative boundaries (Fig. 1B) displayed cohesive tumor fronts where both collagen fibers and α-SMA-positive fibroblasts were predominantly aligned perpendicular to the tumor boundary. Rather than promoting invasion, this perpendicular alignment appeared to reinforce a well-demarcated and continuous interface between the tumor and the surrounding stroma.

Despite these qualitative insights, several fundamental questions remain. A key challenge is understanding how spatio-temporal modifications of the collagen ECM induced by CAFs affect the structural integrity and dissemination of cancer cells. This evaluation is complex and cannot be directly assessed from tissue samples alone. These observations highlight the need for dynamic in vitro assays capable of separating contractile remodeling from enzymatic degradation and resolving how CAF spatial distribution influences ECM remodeling and cancer cell dissemination over time.

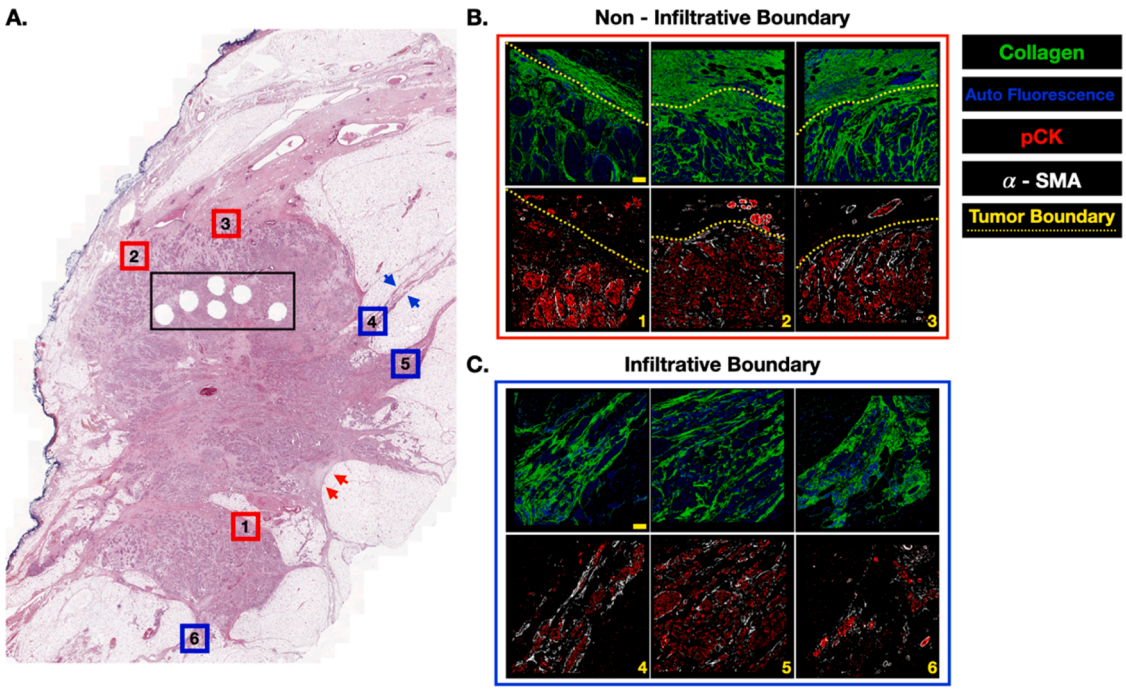

Fig. 1. Infiltrative and Non-Infiltrative TME boundaries can be identified based on cellular organization and collagen architecture.
(A). H&E Stained tissued section of Luminal A tumor. Holes visible at the center of the tumor (black box) are biopsy sections. ROIs boxed in red and blue indicate non-infiltrative and infiltrative tumor boundaries, respectively. Red arrows indicate a non-infiltrative tumor boundary creating a distinct boundary between the tumor core and breast tissue. Blue arrows indicate an infiltrative tumor boundary with collagen fingers protruding into the breast tissue.
(B). Fluorescent scans of non-infiltrative tumor boundaries. On top (red) is the collagen organization at the tumor boundary (yellow dotted line), and below are the scanned sequential tissue slides indicating α-SMA (CAF, white) and pCK (tumor cells, red) organization at the tumor boundary. Scale Bar = 100 μm.
(C). Fluorescent scans of Invasive tumor boundaries. On top (red) is the collagen organization at the tumor boundary, and below are the scanned sequential tissue slides indicating α-SMA (CAF, white) and pCK (tumor cells, red) organization at the tumor boundary.

3.2. 19TT CAFs mediate ECM remodeling and the subsequent MCF7 spheroid expansion and dissemination

To investigate the impact of distinct cellular organization at infiltrative and non-infiltrative tumor fronts on intercellular interactions and ECM remodeling, we co-embedded 19TT CAF and MCF7 cancer cell spheroids within a 3D collagen matrix (3 mg/ml). This assay configuration enabled us to analyze key features observed in tissue sections, such as the interspersed cellular architecture, orientation of collagen fibers, and loose tumor clusters that could interact with 19TT CAF cells, while allowing for kinetic visualization of ECM remodeling (See Fig. 2A, B, D). In this co-culture system, 19TT CAF spheroids maintained direct access to the collagen matrix and engaged with MCF7 tumor spheroids via short-distance migration. Fig. 2(B) and movies 1, 2 and 3 illustrate the spatial organization between 19TT CAF and MCF7 spheroids compared to a single MCF7 spheroid embedded in the collagen matrix. Single MCF7 spheroids displayed gradual, nearly uniform expansion over the entire 48-hour period. However, when 19TT CAF spheroids were seeded less than 200 μm apart from MCF7 spheroids, we observed non-uniform expansion and eventual collapse of MCF7 spheroids. In several samples, we also observed single-cell dissemination from MCF7 spheroids (Fig. 2D, MCF7, 48 hours $d < D_c$). Conversely, when the inter-spheroid distances (d) were greater than 200 μm, MCF7 spheroids exhibited significantly less, yet non-uniform expansion after 48 hours. Based on the distribution of dA (change in MCF7 spheroid area) with respect to distance from 19TT CAF spheroids, we observed a distinct separation between conditions $d < D_c$ and $d \geq D_c$ where D_c (200 μm) was the average MCF7 spheroid diameter (Fig. S3A). In addition, we stimulated MCF7 spheroids with CAF-conditioned medium, and we did not observe any significant spheroid expansion compared with the unstimulated (control condition) MCF7 spheroids (Fig. S4).

To estimate the overall expansion of MCF7 spheroids relative to their initial area was calculated as $dA = (A_{48} - A_0)/A_0$. As shown in Fig. 2 (C), for MCF7 spheroids embedded alone in the collagen matrix, we observed a change in the spheroid area of 1.1 after 48 hours. For 19TT CAF spheroids seeded at a distance $d < D_c$, the mean change in MCF7 spheroid area was 4.1 compared to 1.6 when 19TT CAF spheroids were separated by distances $d > D_c$ (Fig. S3B).

Based on the dynamics captured in Fig. 2B (movies 1, 2 and 3), we identified three key time-dependent interaction patterns (stages) involving 19TT CAFs with both the ECM and MCF7 spheroids. During the first stage (between 4 and 10 hours), 19TT CAF spheroids mechanically engaged with the collagen ECM, remodeling thin fibers into thicker, radially aligned bundles. Image analysis across multiple Z-planes revealed that 19TT CAFs drew collagen fibers from various focal planes, bundling them into radially aligned fibers within the central plane of the spheroids (Fig. S5). This matrix remodeling process likely contributed to increased collagen fiber pixel intensities and deformation of adjacent MCF7 spheroids (Fig. 2B, $d < D_c$) [39,40]. The transition from stage one to stage two was marked by the onset of single-cell dissemination from 19TT CAF spheroids into the surrounding collagen matrix, beginning between 10 and 12 hours and overlapping slightly with the remodeling stage. Disseminating CAFs migrated preferentially into regions that had already undergone mechanical remodeling, where fibers were radially aligned and thickened relative to the unperturbed matrix (Fig. S6). This invasion (t > 10 hours) was accompanied by progressive matrix degradation leading to the formation of central voids and increasing the void fraction of the collagen matrix. The third stage, beginning around 24 hours, was characterized by direct interactions between migrating 19TT CAFs and MCF7 spheroids. The timing of this stage varied with inter-spheroid distances: closer pairs engaged earlier, while those further apart engaged later. Functionally, this phase was marked by non-uniform expansion of MCF7 spheroids, collapse into CAF-generated voids, and frequent single-cell dissemination (Fig. 2D).

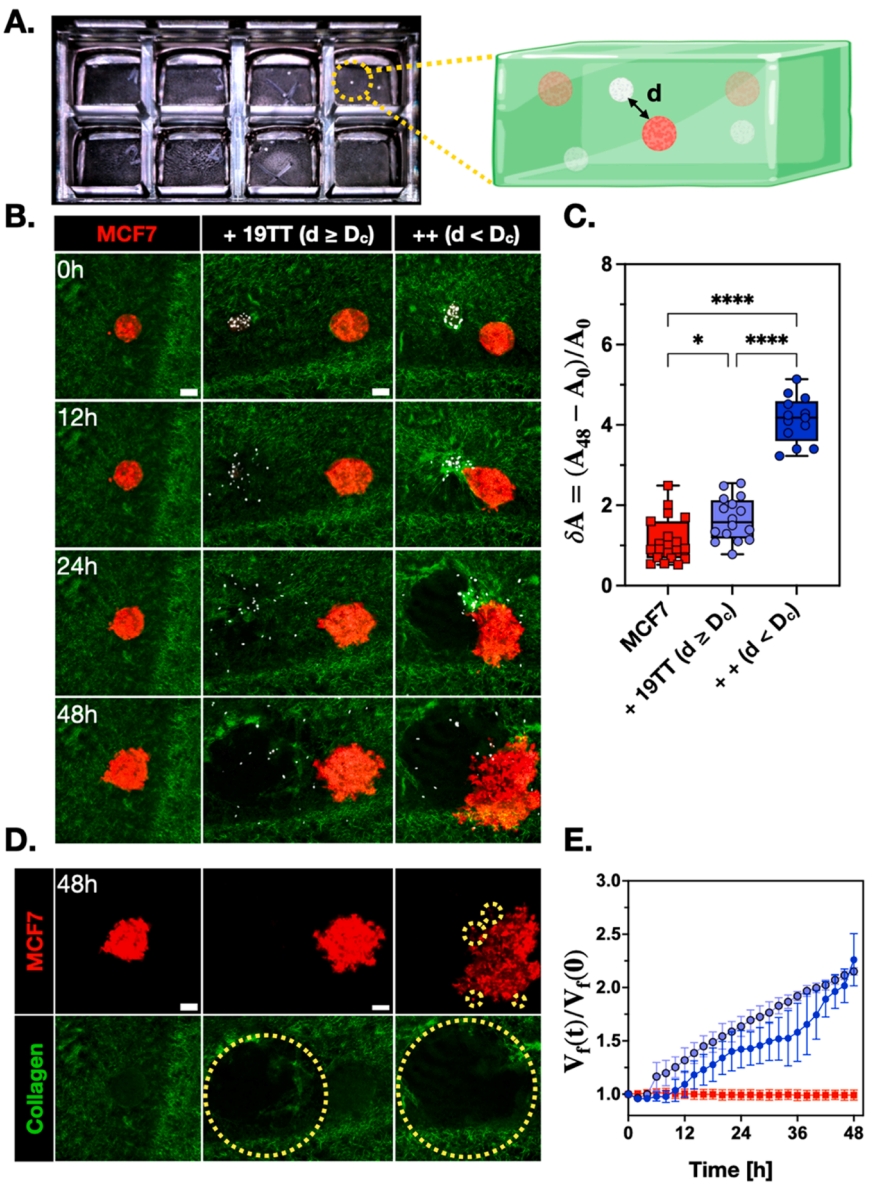

Fig. 2. 19TT CAF - mediated disruption of MCF7 spheroids is dependent on inter-spheroid distance
(A). Ibidi 8-well glass-bottom slide with a 3D collagen matrix containing multicellular tumor spheroids. A zoomed-in schematic represents multicellular luminal MCF7 breast cancer and CAF spheroids embedded in a 3D collagen matrix, separated by a distance "d."
(B). Representative fluorescence images of MCF7 mCherry-labeled cancer cell spheroids (red) and 19TT H2B GFP-labeled CAF spheroids (white) taken at 0-, 24-, and 48-hours post-embedding in a 3 mg/ml rat-tail collagen matrix (green). Spheroids were separated by distances of (ii) 450 μm and (iii) 150 μm.
(C). Quantification of the MCF7 spheroid area was performed under three conditions: when embedded alone (n = 19, N = 3), with 19TT CAF spheroids within 200 μm (n = 13, N = 3), and with 19TT CAF spheroids at distances greater than 200 μm (n = 16, N = 3) after 48 hours (*p < 0.05, ****p < 0.0001).
(D). Overview of (1) single-cell dissemination (yellow circles) observed from MCF7 spheroids and (2) collagen matrix integrity (degraded collagen area in yellow circles) under three conditions: (i) MCF7 alone, (ii) M7 + CAF, $d \geq D_C$, and (iii) M7 + CAF, $d < D_C$, after 48 hours.
(E). Void Fraction ($V_{f(t)}/\ V_{f(0)}$) Quantification of the collagen hydrogel measured from 0 to 48 hours and normalized to its initial value ($V_{f(0)}$) for MCF7 (red), MCF7 + CAF, $d \geq D_C$, (light blue) and (iii) MCF7 + CAF, $d < D_C$ (dark blue).

We further examined MCF7 expansion during the three stages of 19TT CAF and ECM interactions by computing the time-wise evolution $dA = A_t/A_0$. We found that although the MCF7 spheroid expansion is initiated during the mechanical remodeling stage (4 - 10 hours), it is significantly enhanced during the subsequent ECM degradation (t > 10 hours) (Fig. S3B).

To quantify matrix degradation, we calculated the void fraction (V_f) of the collagen matrix through image analysis and normalized to the initial time point. Single MCF7 spheroids showed no detectable degradation, whereas co-cultures with 19TT CAFs displayed a steady increase beginning after ~10 hours, doubling by 48 hours (Fig. 2E). Variability in degradation rates was greater at $d < D_c$ than at $d > D_c$, likely reflecting earlier 19TT CAF-MCF7 interactions at shorter distances, which could attenuate 19TT CAF-mediated collagen remodeling. In contrast, when seeded at greater distances, 19TT CAF spheroids would have been able to remodel the collagen matrix without such interference prior to engaging with MCF7 spheroids. These results confirm that inter-spheroid distance is a critical factor influencing MCF7 spheroid expansion, single-cell dissemination, and the rate of collagen matrix degradation. In the following sections, we will focus our analyses on the 19TT CAF and MCF7 spheroid system where $d < D_c$.

3.3. 19TT CAF spheroid dissemination mediates collagen matrix remodeling and degradation

During 19TT CAF-mediated collagen remodeling, collagen fibers reoriented locally to align radially toward the center of the 19TT CAF spheroid (Fig. 3A, movie 4). To quantify this alignment, we identified and measured the angles of thick collagen fibers relative to the spheroid center (Fig. S1); values approaching 0° indicated stronger alignment. Over the first 10 hours (stage 1), collagen fiber alignment progressively intensified (Fig. 3A-B), with a pronounced peak at 0° by the end of the 10^{th} hour. Concurrently, collagen brightness increased under identical imaging conditions. Pixel intensity analysis confirmed a steady rise during stage 1, consistent with fiber bundling (Fig. 3C). After ~12 hours variability in collagen pixel intensities increased. Dissemination of 19TT CAF single cells (stage 2) began between 8 and 12 hours, suggesting that the remodeled collagen matrix facilitated CAF migration and invasion. Minimal matrix degradation was detected during early matrix remodeling, as reflected by stable values of V_f during the initial 12 hours. At later times, the rate of collagen degradation increased, as evidenced by a steeper slope in the degradation curve (Fig. 3D). By contrast, MCF7-only spheroids showed no significant changes in void fraction or collagen alignment over time, consistent with a lack of intrinsic matrix remodeling capacity in luminal breast cancer cells (Movie 5, Fig. 3A-D) [41].

To test whether collagen matrix remodeling was driven by contractility, we perturbed actomyosin pathways using a direct Myosin II blocker (Bleb) and Rho-associated kinase (ROCK) inhibitor [42,43].

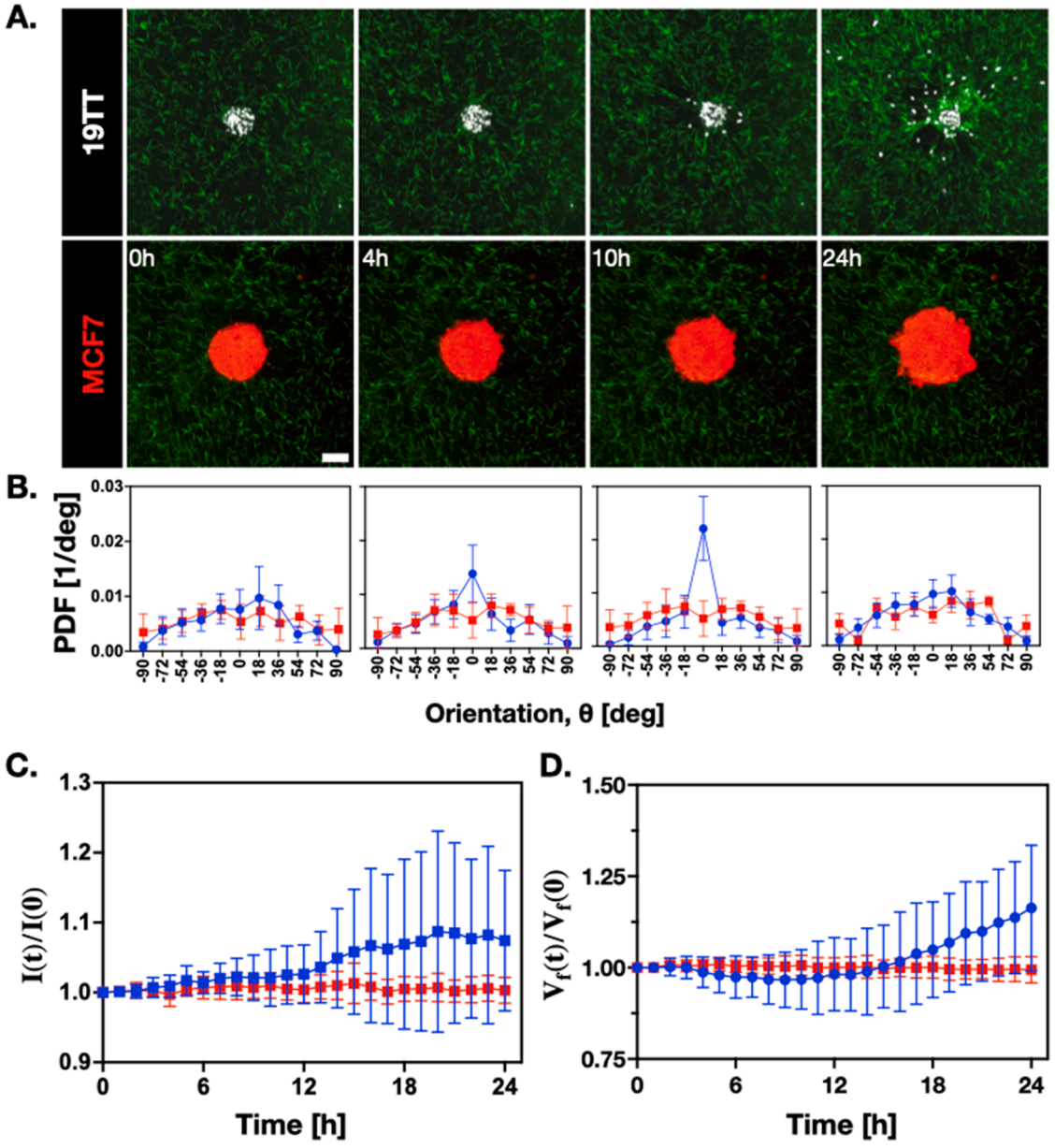

Fig. 3. 19TT CAF spheroid-mediated matrix degradation is preceded by matrix remodeling and fiber reorientation.
(A). Representative time-lapse images of 19TT CAF (white) and MCF7 tumor spheroid (red) in a collagen matrix (green).
(B). Relative collagen fiber orientation concerning the CAF spheroid center in blue (n=11, N = 3) and MCF7 spheroid center in red (n=10, N = 3). Distribution of orientations from -90° to +90° is plotted on the x-axis and the probability density function (PDF) of orientations on the y-axis. Scale bar = 100 μm.
(C). Quantification of collagen V_f during the first 24 hours of the experiment. MCF7 V_f in red and CAF V_f in blue.
(D). Quantification of collagen fiber fluorescence intensities during the first 24 h. Mean pixel intensities of collagen fibers surrounding 19TT CAF and MCF7 spheroids are compared.

Inhibition of Myosin II (Bleb, 10μM) and ROCK (Y27, 10μM) (Fig. S7) confirmed the role of cellular contractility in these early stages. Myosin II inhibition markedly delayed bundling and suppressed early void formation, whereas ROCK inhibition produced thinner but aligned fibers (Fig. S7B). Importantly, in both conditions, CAFs continued to disseminate, and matrix degradation was observed at later times. These results indicate that contractile forces drive early matrix remodeling, while proteolysis sustains later degradation even when contractility is suppressed.

3.4. MMP Inhibition inhibits CAF-mediated matrix degradation but not CAF migration

Next, we investigated the influence of collagen matrix degradation on 19TT CAF invasion and MCF7 spheroid expansion. To inhibit MMP-mediated matrix degradation, we used the broad-spectrum MMP inhibitor Batimastat (BB94) [44]. In comparison to the controls, BB94-treated 19TT CAF spheroids did not degrade the collagen matrix, resulting in no significant change in the void within the matrix over 24 hours (Fig. 4A, BB94 - movie 6, Veh Control - movie 7). Further quantification confirmed this observation: while V_f increased in control conditions, it remained nearly unchanged for CAF spheroids treated with BB94. Despite blocking matrix degradation, BB94 did not prevent collagen remodeling, as we observed thick collagen fibers at 10 hours in both conditions. Orientation analysis likewise showed no major differences between BB94 and controls (Fig. 4B). Collagen pixel intensities also continued to rise under BB94, indicating preserved remodeling activity (Fig. 4C). To assess CAF motility, we calculated the invasive index ($I_V = A_t/A_0 - 1$), defined as the increase in spheroid cross-sectional area (A_t), to quantify migration dynamics. No significant difference was found between treated and control spheroids (Fig. 4D), showing that MMP inhibition had little effect on CAF invasion or single-cell dissemination. Consistent with expectations, MCF7 spheroids alone showed no remodeling under either condition (Fig. S8). Together, these findings confirm that MMP activity drives CAF-mediated degradation but is not required for CAF-driven remodeling or invasion.

We also tested Cathepsin inhibition using a cysteine protease inhibitor (E64, 10 μM) [45]. This treatment marginally reduced collagen degradation compared to control (Fig. S9). The effect was modest compared to the near-complete suppression observed with MMP inhibition, suggesting that cathepsins may contribute to matrix clearance but are not the dominant drivers in this system.

3.5. MMP inhibition reduces MCF7 spheroid expansion but cannot prevent MCF7 cell dissemination

After evaluating MMP inhibition in 19TT CAF spheroids, we expanded our analysis to the MCF7-19TT CAF system. Time-lapse imaging showed that MMP inhibition significantly reduced the expansion of MCF7 spheroids and prevented their disruption at the 48-hour mark compared to the vehicle controls (Fig. 5A-B, and see movies 8, 9). Despite this, MMP inhibition led to an observable increase in single-cell dissemination from MCF7 spheroids within the same timeframe (Fig. 5C). 19TT CAFs maintained their ability to remodel the collagen matrix under BB94 treatment, but MCF7 spheroids no longer displayed the deformations observed in the vehicle controls. In controls, CAF-

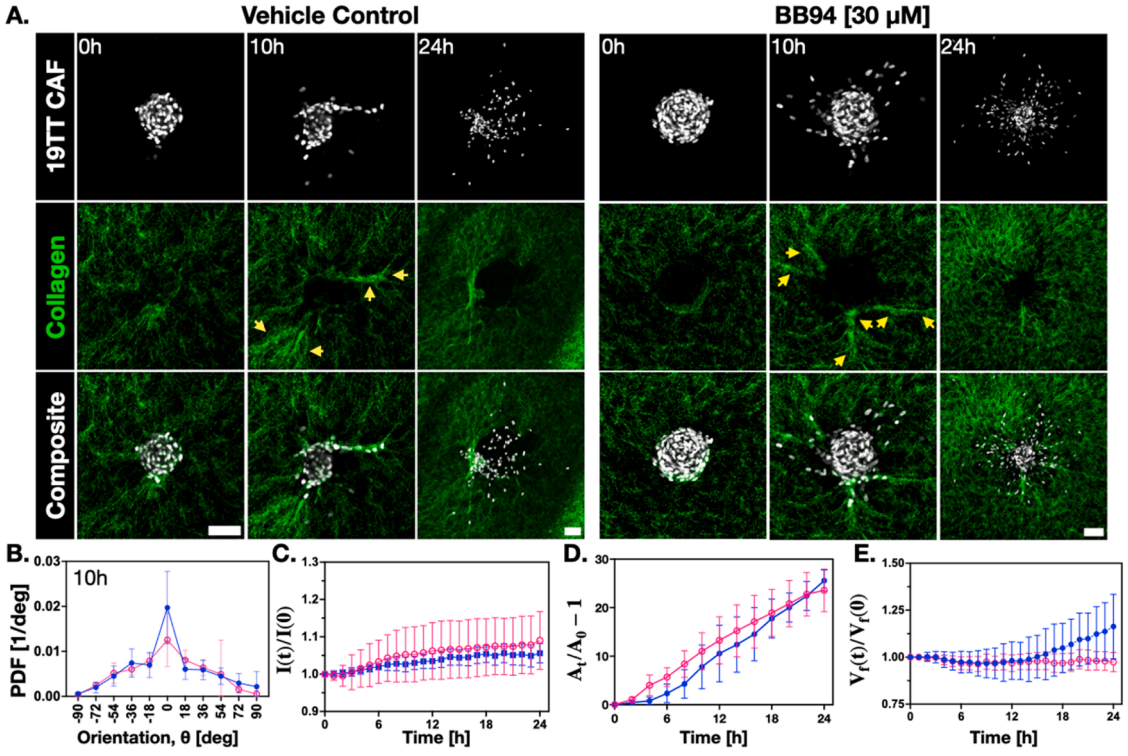

Fig. 4. Broad-spectrum MMP inhibition with Batimastat (BB94, 30μM) attenuates collagen matrix degradation but fails to suppress 19TT CAF invasion or ECM remodeling.

(A). Representative images of 19TT CAF spheroids (white), surrounding collagen matrix (green), and composite overlays under vehicle control and broad-spectrum MMP inhibition (BB94, 30 μM) conditions at 0 and 10 hours. A 24 hour overview highlights migrating CAF cells. Yellow arrows indicate reoriented collagen fibers in vehicle control and MMP inhibition conditions.

(B). Probability density function (PDF) of relative collagen fiber orientation concerning the CAF spheroid center for BB94 treated (pink, n = 8, N = 3) and vehicle control spheroids (blue, n = 8, N = 3) after 10 hours.

(C). Collagen fiber pixel intensities over 24 hours for control (blue) and BB94-treated spheroids (pink).

(D). The invasive index of CAF spheroids was observed 24 hours post-embedding in the collagen matrix under vehicle control and MMP inhibition conditions.

(E). Normalized collagen V_f comparing vehicle control and MMP inhibition conditions over 24 hours.

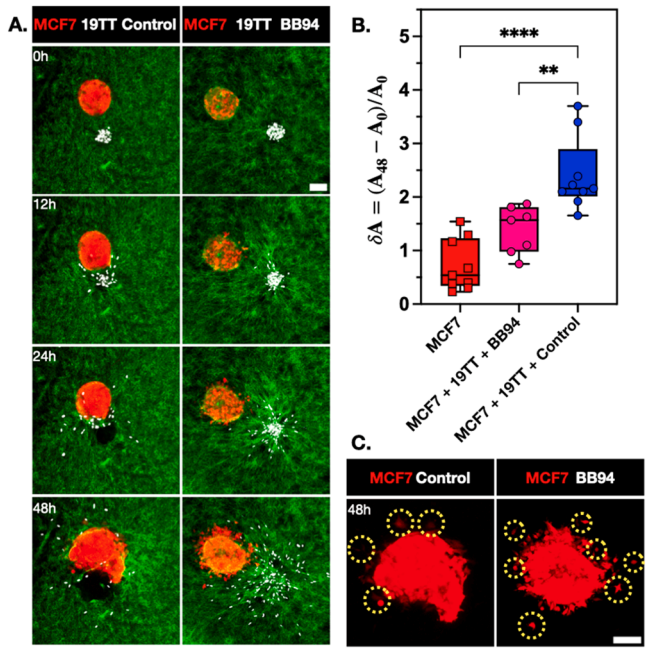

Fig. 5. Broad-spectrum MMP Inhibition with Batimastat (BB-94, 30μM) of the CAF-MCF7 spheroid system reduces MCF7 spheroid expansion but does not prevent single-cell dissemination.
(A). Representative time-lapse images of 19TT CAF spheroids (white) and MCF7 tumor spheroids (red) embedded in a collagen matrix (green) in vehicle control and MMP inhibition conditions.
(B). Quantification of MCF7 spheroid area changes when seeded alone (n = 9, N = 3), vehicle control (n = 9, N = 3) and MMP inhibition conditions after 48 hours (n = 7, N = 3).
(C). Representative images of MCF7 spheroids in vehicle control and broad-spectrum MMP inhibition conditions 48 hours post-embedding in a collagen matrix. Yellow circles highlight single cells disseminating from the spheroids.

mediated remodeling and subsequent degradation deformed the spheroid bulk before triggering expansion and dissemination. By contrast, under MMP inhibition, MCF7 spheroids released single cells isotropically - without prior bulk disruption - during the 48-hour window (Fig. 5C).

3.6. 19TT CAF-MCF7 Heterogeneous spheroids display similar outcomes as dual-spheroid systems

Heterospheroids were designed to model intermixed epithelial-stromal architectures observed in CAF-rich tumor regions, in contrast to the spatially separated dual-spheroid configuration [31,32]. Each heterospheroid contained ~500 MCF7 and 19TT CAFs each, with 19TT CAFs forming a central core surrounded by MCF7 cells (Fig. 6A). After embedding in collagen matrices, time-lapse imaging revealed that 19TT CAF cells remodeled the collagen matrix while largely remaining within the core of the heterospheroid in both control and BB94-treated conditions (Fig. 6A, movies 10, 11). Reoriented collagen bundles were observed around the heterospheroid as early as 12 - 24 hours and remained visible at 30 hours, coinciding with uniform spheroid expansion. Quantifying the relative orientation of collagen fibers in relation to the spheroid center (Fig. 6C) revealed comparable trends between the control and BB94 conditions, yet the degree of reorientation of the collagen fibers after 10 hours was markedly lower compared to the dual-spheroid system (Fig. S10). The expansion of the heterospheroid over the first 48 hours (Fig. 6D) mirrored the behavior observed in the dual-spheroid system, although we noted a greater number of single disseminating cells. Importantly, broad-spectrum MMP inhibition produced results consistent with those observed in the dual-spheroid system, significantly restricting spheroid expansion without affecting collagen fiber reorientation or the dissemination of MCF7 single cells.

4. Discussion

The TME is a dynamic and heterogeneous environment in which CAFs play pivotal roles in promoting invasion through ECM remodeling and degradation. Previous work has largely correlated CAF activity and MMP expression with invasive behavior in patient samples or 2D assays [20,46], but has not resolved how these processes unfold over time in 3D or how they differentially influence cancer cell outcomes. To establish patient relevance, we first analyzed infiltrative and non-infiltrative tumor fronts in luminal breast cancer tissues. Infiltrative regions showed pronounced collagen alignment, elevated α-SMA, and intermixed CAF - cancer cell clusters, whereas non-infiltrative regions displayed weaker collagen alignment, reduced α-SMA, and more segregated tumor-stromal compartments. These observations informed the design of our in vitro models, which can systematically dissect the spatiotemporal principles underlying CAF cancer ECM interactions.

Using a multi-spheroid 3D model coupled with time-lapse imaging, we demonstrate that CAF-mediated remodeling and degradation are temporally and mechanistically separable. During the first stage of matrix remodeling (4-10 hours), CAF spheroids bundled and reoriented fibrillar collagen into thick aligned fibers, thereby preparing the matrix for subsequent invasion and degradation. This early, contractility-driven remodeling facilitated deformation of adjacent MCF7 spheroids and, in many cases, early single-cell dissemination. Contractile forces exerted by 19TT CAFs also likely contributed to the increased pixel intensity of collagen fibers [39,40]. Following matrix reorganization, 19TT CAF migration commenced and was accompanied by progressive matrix degradation, as indicated by increasing void formation over the subsequent 24 hours. The protease-dependent matrix degradation was only detectable after ~10-12 hours, coinciding with increased void fraction and supporting bulk MCF7 spheroid expansion. However, the matrix degradation rate plateaued between 24 and 36 hours, likely coinciding with 19TT CAF-MCF7 interactions. After 36 hours, the degradation reaccelerated as 19TT CAFs migrated deeper into the matrix, having already disrupted the MCF7 spheroids. These observations highlight the spatiotemporal adaptability of 19TT CAFs in ECM remodeling to facilitate tumor invasion. Proximity of 19TT CAFs to MCF7 spheroids was a critical determinant of tumor expansion and dissemination, with spheroids located within one D_C of a 19TT CAF spheroid experiencing significantly increased expansion and single-cell dissemination compared to those positioned further away. Taken together, these data explicitly delineate the temporal and functional contributions of CAF-mediated ECM remodeling and degradation. Remodeling, defined as contractility-driven collagen bundling, occurred within the first 4-10 hours and facilitated MCF7 spheroid deformation and early single-cell dissemination. By contrast, degradation, detectable only after ~10-12 hours, was protease-dependent and primarily supported bulk spheroid expansion.

Spatial organization further modulated these temporal dynamics. In dual-spheroid systems, remodeling and degradation occurred sequentially, whereas in heterospheroids, with intermixed CAFs and cancer cells - reflecting the intermixed epithelial-stromal architecture observed in CAF-rich tumor regions [31,32] - both processes occurred concurrently. These findings parallel research observations that epithelial-stromal proximity accelerates invasion [7,47], while also providing mechanistic insight into how architectural context shapes invasion modes.

To inhibit matrix degradation, we employed a broad-spectrum MMP inhibitor. MMP inhibition effectively prevented collagen degradation without impairing 19TT CAF motility or ECM remodeling. Under these conditions, MCF7 spheroid expansion was markedly reduced, whereas single-cell dissemination persisted or was even enhanced. This reinforces that bulk expansion depends on matrix degradation, whereas

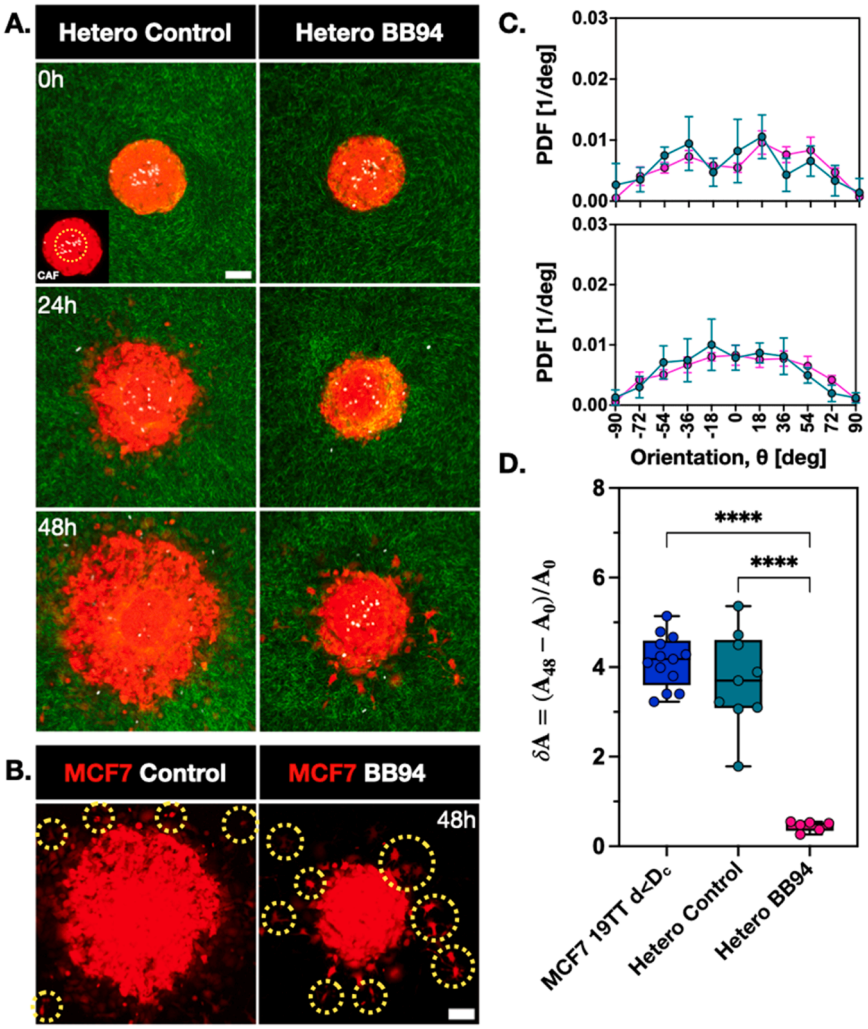

Fig. 6. Heterospheroids (19TT CAF – MCF7) show similar expansion rates and single cell dissemination as MCF7 spheroids when seeded close to CAF spheroids.
(A). Representative time-lapse images of heterospheroids composed of MCF7 tumor cells (red) and 19TT CAFs (white) embedded in a 3D collagen matrix (green). Shown are vehicle control and BB94 (30 μM) treated spheroids. The inset highlights a heterospheroid, with 19TT CAF cells located centrally (yellow circle). Scale bar = 100 μm.
(B). Representative images of MCF7 cells in vehicle control and BB94-treated conditions 48 hours post-embedding in the collagen matrix. Yellow circles highlight single cells disseminating from the spheroids.
(C). Collagen fiber orientation with respect to heterogenous spheroid center at 0 and 24 hours, respectively. Control in green (n = 9, N = 3) and MMP inhibition in pink (n = 6, N = 3)
(D). Quantifying heterogeneous spheroid area changes under vehicle control and MMP inhibition conditions after 48 hours.

dissemination can proceed independently of it. Since MMP inhibition did not hinder CAF-driven remodeling, contractile forces likely create interstitial spaces that support dissemination. Further analysis confirmed the absence of matrix degradation in MMP-inhibited samples (Fig. 4E). Consistent with prior work, ECM architecture dictates migration mode: dense matrices promote single-cell dissemination, while looser matrices favor collective invasion [39,48–53]. Our results thus show that CAF-driven invasion operates through two separable mechanisms: contractility-dependent collagen remodeling and protease-mediated degradation. Collagen matrix remodeling supports single cell dissemination, while matrix degradation supports bulk expansion and disruption of the cancer cell spheroid. This mechanistic dissection helps explain why MMP inhibitors have shown limited clinical efficacy and highlights the need to target both proteolytic and mechanical CAF activities. The differential effects of contractility and protease inhibition on collagen organization, void formation, and CAF behavior are summarized in Table S1, providing a concise overview of how each pathway contributes to distinct stages of matrix remodeling and invasion dynamics.

While our study emphasizes on ECM remodeling and degradation, CAFs also play broader roles in vivo, including ECM production, immune modulation, and metabolic support [12]. The 19TT CAF line used here represents a contractile, desmoplastic subtype particularly relevant to invasive tumor fronts. Future studies incorporating additional CAF subtypes and tumor contexts will be important for validating and expanding these insights. Together these results also suggest that the cell dissemination observed under control conditions is a combination of both proteolytic and non-proteolytic migration modes. Additional future dissection of these routes is warranted to assess adhesion dependence, confinement sensitivity, and morphology-based kinematics (sphericity, cell speed, etc.). Beyond mechanistic insight, our findings also point to therapeutic strategies that disrupt CAF-mediated remodeling, such as combining inhibitors of actomyosin contractility with agents targeting collagen crosslinking enzymes, such as lysyl oxidase (LOX), which reduces matrix stiffening and tumor progression in preclinical models [54]. Such approaches could complement conventional MMP inhibition

and provide a more comprehensive framework to mitigate CAF-driven invasion and resistance.

5. Conclusion

This study elucidates the spatiotemporal dynamics of CAF-driven ECM remodeling and its dual role in tumor invasion (focused on the indolent breast cancer type), revealing valuable mechanistic insights into the interplay between stromal activity and tumor progression. Our findings demonstrate that CAFs orchestrate a sequential cascade of ECM reorganization, migration, and degradation, which collectively enable tumor spheroid disruption and dissemination. The initial phase of collagen fiber alignment and bundling by CAFs creates a permissive microenvironment for subsequent invasion, while MMP-mediated degradation facilitates bulk tumor expansion. Notably, MMP inhibition experiments revealed that ECM remodeling alone - via CAF contractility - is sufficient to generate interstitial spaces for single-cell dissemination, decoupling this process from matrix degradation. These results may also shed some light on the limited success MMP inhibitors have had in clinical settings as cancer therapeutics. Additionally, translating these insights into strategies to inhibit CAF-mediated matrix remodeling and subsequent CAF migration could offer novel avenues for metastasis prevention.

CRediT authorship contribution statement

Pranav Mehta: Writing – original draft, Visualization, Methodology, Investigation, Formal analysis, Data curation, Conceptualization. **Ankur Deep Bordoloi:** Visualization, Validation, Software, Methodology, Formal analysis, Conceptualization, Writing – review & editing, Supervision. **Cor Ravensbergen:** Formal analysis, Data curation, Conceptualization. **Ma.Kristen H. David:** Data curation. **Wilma Mesker:** Resources. **Gerrit Jan Liefers:** Resources. **Peter ten Dijke:** Writing – review & editing, Supervision, Resources, Methodology, Investigation, Funding acquisition, Conceptualization. **Pouyan E. Boukany:** Writing – review & editing, Supervision, Resources, Project administration, Investigation, Funding acquisition, Conceptualization.

Declaration of competing interest

The authors declare that they have no known competing financial interests or personal relationships that could have appeared to influence the work reported in this paper.

Acknowledgements

P.T.D., and P.E.B. gratefully acknowledge funding from the Delft Health Technology grant (between LUMC and TU Delft) and ZonMW grant (09120012010061). A.D.B. gratefully acknowledges funding from MSCA Postdoctoral Fellowships 2022 Project ID: 101111247.

Supplementary materials

Supplementary material associated with this article can be found, in the online version, at doi:10.1016/j.actbio.2025.11.027.

References

[1] L. Wilkinson, T. Gathani, Understanding breast cancer as a global health concern, Br. J. Radiol. 95 (2021) 20211033, https://doi.org/10.1259/BJR.20211033, 20211033.
[2] F. Lüönd, S. Tiede, G. Christofori, Breast cancer as an example of tumour heterogeneity and tumour cell plasticity during malignant progression, Br. J. Cancer 125 (2021) 164–175, https://doi.org/10.1038/s41416-021-01328-7.
[3] A. Muchlińska, A. Nagel, M. Popęda, J. Szade, M. Niemira, J. Zieliński, J. Skokowski, N. Bednarz-Knoll, A.J. Żaczek, Alpha-smooth muscle actin-positive cancer-associated fibroblasts secreting osteopontin promote growth of luminal breast cancer, Cell. Mol. Biol. Lett. 27 (2022) 1–14, https://doi.org/10.1186/S11658-022-00351-7/FIGURES/3.
[4] G.W. van Pelt, T.P. Sandberg, H. Morreau, H. Gelderblom, J.H.J.M. van Krieken, R. A.E.M. Tollenaar, W.E. Mesker, The tumour–stroma ratio in colon cancer: the biological role and its prognostic impact, Histopathology 73 (2018) 197–206, https://doi.org/10.1111/HIS.13489.
[5] M. Xu, T. Zhang, R. Xia, Y. Wei, X. Wei, Targeting the tumor stroma for cancer therapy, Mol. Cancer 21 (1) (2022) 1–38, https://doi.org/10.1186/S12943-022-01670-1, 21 (2022).
[6] D. Yan, X. Ju, B. Luo, F. Guan, H. He, H. Yan, J. Yuan, Tumour stroma ratio is a potential predictor for 5-year disease-free survival in breast cancer, BMC. Cancer 22 (2022) 1–11, https://doi.org/10.1186/S12885-022-10183-5/FIGURES/4.
[7] N.M. Atallah, N. Wahab, M.S. Toss, S. Makhlouf, A.Y. Ibrahim, A.G. Lashen, S. Ghannam, N.P. Mongan, M. Jahanifar, S. Graham, M. Bilal, A. Bhalerao, S. E. Ahmed Raza, D. Snead, F. Minhas, N. Rajpoot, E. Rakha, Deciphering the morphology of tumor-stromal features in invasive breast cancer using artificial intelligence, Mod. Pathol. 36 (2023) 100254, https://doi.org/10.1016/J.MODPAT.2023.100254, 100254.
[8] J. Wu, C. Liang, M. Chen, W. Su, Association between tumor-stroma ratio and prognosis in solid tumor patients: a systematic review and meta-analysis, Oncotarget. 7 (2016) 68954, https://doi.org/10.18632/ONCOTARGET.12135, 68954.
[9] R.M. Bremnes, T. Dønnem, S. Al-Saad, K. Al-Shibli, S. Andersen, R. Sirera, C. Camps, I. Marinez, L.T. Busund, The role of tumor stroma in cancer progression and prognosis: emphasis on carcinoma-associated fibroblasts and non-small cell lung cancer, J. Thorac. Oncol. 6 (2011) 209–217, https://doi.org/10.1097/JTO.0B013E3181F8A1BD.
[10] N. Pasha, N.C. Turner, Understanding and overcoming tumor heterogeneity in metastatic breast cancer treatment, Nat. Cancer 2 (2021), https://doi.org/10.1038/s43018-021-00229-1.
[11] B. Bareham, M. Dibble, M. Parsons, Defining and modeling dynamic spatial heterogeneity within tumor microenvironments, Curr. Opin. Cell Biol. 90 (2024) 102422, https://doi.org/10.1016/J.CEB.2024.102422, 102422.
[12] G. Friedman, O. Levi-Galibov, E. David, C. Bornstein, A. Giladi, M. Dadiani, A. Mayo, C. Halperin, M. Pevsner-Fischer, H. Lavon, S. Mayer, R. Nevo, Y. Stein, N. Balint-Lahat, I. Barshack, H.R. Ali, C. Caldas, E. Nili-Gal-Yam, U. Alon, I. Amit, R. Scherz-Shouval, Cancer-associated fibroblast compositions change with breast cancer progression linking the ratio of S100A4+ and PDPN+ CAFs to clinical outcome, Nat. Cancer 1 (2020) 692–708, https://doi.org/10.1038/s43018-020-0082-y.
[13] S.E. Reid, J. Pantaleo, P. Bolivar, M. Bocci, J. Sjölund, M. Morsing, E. Cordero, S. Larsson, M. Malmberg, B. Seashore-Ludlow, K. Pietras, Cancer-associated fibroblasts rewire the estrogen receptor response in luminal breast cancer, enabling estrogen independence, Oncogene 43 (2024) 1113–1126, https://doi.org/10.1038/S41388-024-02973-X.
[14] K.F. Goliwas, S. Libring, E. Berestesky, S. Gholizadeh, S.C. Schwager, A.R. Frost, T. R. Gaborski, J. Zhang, C.A. Reinhart-King, Mitochondrial transfer from cancer-associated fibroblasts increases migration in aggressive breast cancer, J. Cell Sci. 136 (2023), https://doi.org/10.1242/JCS.260419/VIDEO-3.
[15] N.I. Nissen, M. Karsdal, N. Willumsen, Collagens and Cancer associated fibroblasts in the reactive stroma and its relation to cancer biology, J. Experim. Clin. Cancer Res. 38 (2019) 1–12, https://doi.org/10.1186/S13046-019-1110-6/TABLES/1.
[16] J. Barbazán, D.Matic Vignjevic, Cancer associated fibroblasts: is the force the path to the dark side? Curr. Opin. Cell Biol. 56 (2019) 71–79, https://doi.org/10.1016/J.CEB.2018.09.002.
[17] D. Pankova, Y. Chen, M. Terajima, M.J. Schliekelman, B.N. Baird, M. Fahrenholtz, L. Sun, B.J. Gill, T.J. Vadakkan, M.P. Kim, Y.H. Ahn, J.D. Roybal, X. Liu, E.R. P. Cuentas, J. Rodriguez, I.I. Wistuba, C.J. Creighton, D.L. Gibbons, J.M. Hicks, M. E. Dickinson, J.L. West, K.J. Grande-Allen, S.M. Hanash, M. Yamauchi, J.M. Kurie, Cancer-associated fibroblasts induce a collagen cross-link switch in tumor stroma, Mol. Cancer Res.: MCR 14 (2015) 287, https://doi.org/10.1158/1541-7786.MCR-15-0307, 287.
[18] B. Erdogan, D.J. Webb, Cancer-associated fibroblasts modulate growth factor signaling and extracellular matrix remodeling to regulate tumor metastasis, Biochem. Soc. Trans. 45 (2017) 229–236, https://doi.org/10.1042/BST20160387.
[19] L. Liu, H. Yu, H. Zhao, Z. Wu, Y. Long, J. Zhang, X. Yan, Z. You, L. Zhou, T. Xia, Y. Shi, B. Xiao, Y. Wang, C. Huang, Y. Du, Matrix-transmitted paratensile signaling enables myofibroblast-fibroblast cross talk in fibrosis expansion, Proc. Natl. Acad. Sci. u S. a 117 (2020) 10832–10838, https://doi.org/10.1073/PNAS.1910650117/SUPPL_FILE/PNAS.1910650117.SM08.MP4.
[20] H. Li, Z. Qiu, F. Li, C. Wang, The relationship between MMP-2 and MMP-9 expression levels with breast cancer incidence and prognosis, Oncol. Lett. 14 (2017) 5865–5870, https://doi.org/10.3892/OL.2017.6924/HTML.
[21] H. Su, M. Karin, M. Karin, Collagen architecture and signaling orchestrate cancer development, Trends. Cancer 9 (2023) 764–773, https://doi.org/10.1016/j.trecan.2023.06.002.
[22] B.K. Patel, K. Pepin, K.R. Brandt, G.L. Mazza, B.A. Pockaj, J. Chen, Y. Zhou, D. W. Northfelt, K. Anderson, J.M. Kling, C.M. Vachon, K.R. Swanson, M. Nikkhah, R. Ehman, Association of breast cancer risk, density, and stiffness: global tissue stiffness on breast MR elastography (MRE), Breast. Cancer Res. Treat. 194 (2022) 79, https://doi.org/10.1007/S10549-022-06607-2, 79.
[23] F. Calvo, N. Ege, A. Grande-Garcia, S. Hooper, R.P. Jenkins, S.I. Chaudhry, K. Harrington, P. Williamson, E. Moeendarbary, G. Charras, E. Sahai, Mechanotransduction and YAP-dependent matrix remodelling is required for the generation and maintenance of cancer-associated fibroblasts, Nat. Cell Biol. 15 (6) (2013) 637–646, https://doi.org/10.1038/ncb2756, 15 (2013).

[24] A.K. Simi, M.F. Pang, C.M. Nelson, Extracellular matrix stiffness exists in a feedback loop that drives tumor progression, Adv. Exp. Med. Biol. 1092 (2018) 57–67, https://doi.org/10.1007/978-3-319-95294-9_4/FIGURES/2.
[25] K.M. Riching, B.L. Cox, M.R. Salick, C. Pehlke, A.S. Riching, S.M. Ponik, B.R. Bass, W.C. Crone, Y. Jiang, A.M. Weaver, K.W. Eliceiri, P.J. Keely, 3D collagen alignment limits protrusions to enhance breast cancer cell persistence, Biophys. J. 107 (2015) 2546–2558, https://doi.org/10.1016/j.bpj.2014.10.035.
[26] P.P. Provenzano, D.R. Inman, K.W. Eliceiri, S.M. Trier, P.J. Keely, Contact guidance mediated three-dimensional cell migration is regulated by Rho/ROCK-dependent matrix reorganization, Biophys. J. 95 (2008) 5374–5384, https://doi.org/10.1529/biophysj.108.133116.
[27] P.P. Provenzano, K.W. Eliceiri, J.M. Campbell, D.R. Inman, J.G. White, P.J. Keely, Collagen reorganization at the tumor-stromal interface facilitates local invasion, BMC. Med. 4 (2006) 1–15, https://doi.org/10.1186/1741-7015-4-38/FIGURES/7.
[28] S.V. Bayer, W.R. Grither, A. Brenot, P.Y. Hwang, C.E. Barcus, M. Ernst, P. Pence, C. Walter, A. Pathak, G.D. Longmore, DDR2 controls breast tumor stiffness and metastasis by regulating integrin mediated mechanotransduction in cafs, Elife 8 (2019), https://doi.org/10.7554/ELIFE.45508.
[29] A. Marusyk, D.P. Tabassum, M. Janiszewska, A.E. Place, A. Trinh, A.I. Rozhok, S. Pyne, J.L. Guerriero, S. Shu, M. Ekram, A. Ishkin, D.P. Cahill, Y. Nikolsky, T. A. Chan, M.F. Rimawi, S. Hilsenbeck, R. Schiff, K.C. Osborne, A. Letai, K. Polyak, Spatial proximity to fibroblasts impacts molecular features and therapeutic sensitivity of breast cancer cells influencing clinical outcomes, Cancer Res. 76 (2016) 6495–6506, https://doi.org/10.1158/0008-5472.CAN-16-1457.
[30] Y. Wu, Y. Shi, Z. Luo, X. Zhou, Y. Chen, X. Song, S. Liu, Spatial multi-omics analysis of tumor-stroma boundary cell features for predicting breast cancer progression and therapy response, Front. Cell Dev. Biol. 13 (2025) 1570696, https://doi.org/10.3389/fcell.2025.1570696.
[31] S. Jing, D. Liu, N. Feng, H. Dong, H. Wang, X. Yan, X. Chen, M. Qu, P. Lin, B. Yi, F. Feng, L. Chen, H. Wang, H. Li, Y. He, Spatial multiomics reveals a subpopulation of fibroblasts associated with cancer stemness in human hepatocellular carcinoma, Genome Med. 16 (2024) 98, https://doi.org/10.1186/s13073-024-01367-8.
[32] A. Forsthuber, B. Aschenbrenner, A. Korosec, T. Jacob, K. Annusver, N. Krajic, D. Kholodniuk, S. Frech, S. Zhu, K. Purkhauser, K. Lipp, F. Werner, V. Nguyen, J. Griss, W. Bauer, A. Soler Cardona, B. Weber, W. Weninger, B. Gesslbauer, C. Staud, J. Nedomansky, C. Radtke, S.N. Wagner, P. Petzelbauer, M. Kasper, B. M. Lichtenberger, Cancer-associated fibroblast subtypes modulate the tumor-immune microenvironment and are associated with skin cancer malignancy, Nat. Commun. 15 (2024) 9678, https://doi.org/10.1038/s41467-024-53908-9.
[33] A. Sieuwerts, J. Bolt-de Vries, P. Bosma, S. Swiggers, J. Klijn, J. Foekens, J. Martens, Aging of stromal-derived human breast fibroblasts might contribute to breast cancer progression, Thromb. Haemost. 89 (2003) 393–404, https://doi.org/10.1055/s-0037-1613457.
[34] J. Ren, M. Smid, J. Iaria, D.C.F. Salvatori, H. Van Dam, H.J. Zhu, J.W.M. Martens, P.Ten Dijke, Cancer-associated fibroblast-derived Gremlin 1 promotes breast cancer progression, Breast Cancer Res.: BCR 21 (2019) 109, https://doi.org/10.1186/S13058-019-1194-0, 109.
[35] H.P.H. Naber, E. Wiercinska, P.T. Dijke, T. van Laar, Spheroid assay to measure TGF-β-induced invasion, J. Visual. Exper.: JoVE (2011) 3337, https://doi.org/10.3791/3337, 3337.
[36] V. Padmanaban, E.M. Grasset, N.M. Neumann, A.K. Fraser, E. Henriet, W. Matsui, P.T. Tran, K.J. Cheung, D. Georgess, A.J. Ewald, Organotypic culture assays for murine and human primary and metastatic-site tumors, Nat. Protoc. 15 (2020) 2413, https://doi.org/10.1038/S41596-020-0335-3, 2413.
[37] N. Otsu, A threshold selection method from gray-level histograms, IEEE Trans. Syst. Man Cybern. 9 (1979) 62–66, https://doi.org/10.1109/TSMC.1979.4310076.
[38] R. Rezakhaniha, A. Agianniotis, J.T.C. Schrauwen, A. Griffa, D. Sage, C.V. C. Bouten, F.N. van de Vosse, M. Unser, N. Stergiopulos, Experimental investigation of collagen waviness and orientation in the arterial adventitia using confocal laser scanning microscopy, Biomech. Model. Mechanobiol. 11 (2012) 461–473, https://doi.org/10.1007/s10237-011-0325-z.
[39] D. Böhringer, A. Bauer, I. Moravec, L. Bischof, D. Kah, C. Mark, T.J. Grundy, E. Görlach, G.M. O'neill, S. Budday, P. Strissel, R. Strick, A. Malandrino, R. Gerum, M. Mak, M. Rausch, B. Fabry, Fiber alignment in 3D collagen networks as a biophysical marker for cell contractility, (n.d.). https://doi.org/10.1101/2023.06.28.546896.
[40] L.M. Jawerth, S. Münster, D.A. Vader, B. Fabry, D.A. Weitz, A blind spot in confocal reflection microscopy: the dependence of fiber brightness on fiber orientation in imaging biopolymer networks, Biophys. J. 98 (2010) L1–L3, https://doi.org/10.1016/j.bpj.2009.09.065.
[41] M.J. Ziperstein, A. Guzman, L.J. Kaufman, Breast cancer cell line aggregate morphology does not predict invasive capacity, PLoS. One 10 (2015) e0139523, https://doi.org/10.1371/journal.pone.0139523.
[42] M. Kovács, J. Tóth, C. Hetényi, A. Málnási-Csizmadia, J.R. Sellers, Mechanism of blebbistatin inhibition of Myosin II, J. Biol. Chem. 279 (2004) 35557–35563, https://doi.org/10.1074/jbc.M405319200.
[43] K. Kuwahara, Y. Saito, O. Nakagawa, I. Kishimoto, M. Harada, E. Ogawa, Y. Miyamoto, I. Hamanaka, N. Kajiyama, N. Takahashi, T. Izumi, R. Kawakami, N. Tamura, Y. Ogawa, K. Nakao, The effects of the selective ROCK inhibitor, Y27632, on ET-1-induced hypertrophic response in neonatal rat cardiac myocytes – possible involvement of Rho/ROCK pathway in cardiac muscle cell hypertrophy, FEBS Lett. 452 (1999) 314–318, https://doi.org/10.1016/S0014-5793(99)00680-8.
[44] B. Davies, P.D. Brown, N. East, M.J. Crimmin, F.R. Balkwill, A synthetic matrix metalloproteinase inhibitor decreases tumor burden and prolongs survival of mice bearing human ovarian carcinoma xenografts, Cancer Res. 53 (1993) 2087–2091.
[45] K. Matsumoto, K. Mizoue, K. Kitamura, W.-C. Tse, C.P. Huber, T. Ishida, Structural basis of inhibition of cysteine proteases by E-64 and its derivatives, Biopolymers 51 (1999) 99–107.
[46] H. Huang, Matrix metalloproteinase-9 (MMP-9) as a cancer biomarker and MMP-9 biosensors: recent advances, Sens. (Switzerland) 18 (2018) 5–7, https://doi.org/10.3390/s18103249.
[47] K. Lisek, I. Theurillat, T.M. Pentimalli, S. Beier, D. León-Periñán, A. Antonatou, S. Dubnov, M. Müller, F. Hubl, A. Xhuri, H. Romanowicz, B. Smolarz, E. Montaudon, S. Raimundo, A. Margineanu, M. Schott, S. Kunz, E. Marangoni, N. Karaiskos, M. Nitzan, W. Birchmeier, N. Rajewsky, Spatiotemporal dynamics of tumor microenvironment remodeling, (2025). https://doi.org/10.1101/2025.07.15.662972.
[48] A. van der Net, Z. Rahman, A.D. Bordoloi, I. Muntz, P. Ten Dijke, P.E. Boukany, G. H. Koenderink, EMT-related cell-matrix interactions are linked to states of cell unjamming in cancer spheroid invasion, iScience 27 (2024) 111424, https://doi.org/10.1016/j.isci.2024.111424.
[49] C.D. Paul, P. Mistriotis, K. Konstantopoulos, Cancer cell motility: lessons from migration in confined spaces, Nat. Rev. Cancer 17 (2017) 131–140, https://doi.org/10.1038/nrc.2016.123.
[50] B. Trappmann, B.M. Baker, W.J. Polacheck, C.K. Choi, J.A. Burdick, C.S. Chen, Matrix degradability controls multicellularity of 3D cell migration, Nat. Commun. 8 (2017) 1–8, https://doi.org/10.1038/s41467-017-00418-6.
[51] O. Ilina, P. Friedl, Mechanisms of collective cell migration at a glance, J. Cell Sci. 122 (2009) 3203–3208, https://doi.org/10.1242/jcs.036525.
[52] Z. Rahman, A.D. Bordoloi, H. Rouhana, M. Tavasso, G. van der Zon, V. Garbin, P. ten Dijke, P.E. Boukany, Interstitial flow potentiates TGF-β/smad-signaling activity in lung cancer spheroids in a 3D-microfluidic chip, Lab. Chip. 24 (2024) 422–433, https://doi.org/10.1039/D3LC00886J.
[53] O. Ilina, P.G. Gritsenko, S. Syga, J. Lippoldt, C.A.M. La Porta, O. Chepizhko, S. Grosser, M. Vullings, G.J. Bakker, J. Starruß, P. Bult, S. Zapperi, J.A. Käs, A. Deutsch, P. Friedl, Cell–cell adhesion and 3D matrix confinement determine jamming transitions in breast cancer invasion, Nat. Cell Biol. 22 (2020) 1103–1115, https://doi.org/10.1038/s41556-020-0552-6.
[54] T. Koorman, K.A. Jansen, A. Khalil, P.D. Haughton, D. Visser, M.A.K. Rätze, W. E. Haakma, G. Sakalauskaitè, P.J. van Diest, J. de Rooij, P.W.B. Derksen, Spatial collagen stiffening promotes collective breast cancer cell invasion by reinforcing extracellular matrix alignment, Oncogene 41 (17) (2022) 2458–2469, https://doi.org/10.1038/s41388-022-02258-1, 41 (2022).